

Tailoring FeN₄ Sites with Edge Enrichment for Boosted Oxygen Reduction Performance in Proton Exchange Membrane Fuel Cell

Xiaogang Fu, Na Li, Bohua Ren, Gaopeng Jiang, Yanru Liu, Fathy M. Hassan, Dong Su,* Jianbing Zhu, Lin Yang, Zhengyu Bai,* Zachary P. Cano, Aiping Yu, and Zhongwei Chen*

Transition metal atoms with corresponding nitrogen coordination are widely proposed as catalytic centers for the oxygen reduction reaction (ORR) in metal–nitrogen–carbon (M–N–C) catalysts. Here, an effective strategy that can tailor Fe–N–C catalysts to simultaneously enrich the number of active sites while boosting their intrinsic activity and utilization is reported. This is achieved by edge engineering of FeN₄ sites via a simple ammonium chloride salt-assisted approach, where a high fraction of FeN₄ sites are preferentially generated and hosted in a graphene-like porous scaffold. Theoretical calculations reveal that the FeN₄ moieties with adjacent pore defects are likely to be more active than the nondefective configuration. Coupled with the facilitated accessibility of active sites, this prepared catalyst, when applied in a practical H₂–air proton exchange membrane fuel cell, delivers a remarkable peak power density of 0.43 W cm⁻², ranking it as one of the most active M–N–C catalysts reported to date. This work provides a new avenue for boosting ORR activity by edge manipulation of FeN₄ sites.

Proton exchange membrane fuel cells (PEMFCs) fueled by renewable hydrogen are attractive and promising devices to provide sustainable and clean energy.^[1] However, a major drawback of current PEMFC technology is their high cost, in large part due to the use of platinum-based catalysts, especially in catalyzing the inherently sluggish oxygen reduction reaction (ORR) process at the cathode.^[2] Pyrolyzed carbon materials incorporated with inexpensive transition metals (e.g., Fe and Co) and nitrogen (metal–nitrogen–carbon (M–N–C)) represent the most promising candidates to potentially substitute Pt-based catalysts in PEMFCs.^[3] Recent studies have suggested that metal atoms with corresponding N-coordinations (denoted as MN_x moieties) hosted within a carbon matrix can serve as catalytic centers

for ORR.^[4] However, despite numerous efforts to date, designing highly active M–N–C catalysts through tailoring MN_x sites remains challenging. Above all, the high temperature pyrolysis process inevitably generates a significant amount of less active or inactive metal-based aggregates (e.g., metallic iron, iron carbide, oxide, and sulfide) alongside active MN_x moieties.^[5] Thus, maximizing the formation of MN_x moieties and minimizing other metal-based phases with a rational design strategy is greatly desired. Second, in parallel with efforts to increase the proportion of MN_x sites, boosting their intrinsic activity is also critical to enhance the overall catalytic efficiency.^[6] In this regard, much attention has been paid to identify more active MN_x coordination configurations;^[4b,c,7] however, the interactive catalytic contribution of the neigh-

boring carbon atoms has received less focus and needs further exploration. Lastly, to further improve the ORR performance in fuel cells, catalysts possessing an open porous architecture are absolutely desired to facilitate the accessibility and enhance the utilization of MN_x moieties.^[8] Thus far, a simple and controllable pore construction approach to achieve this structure has yet to be explored for Fe–N–C catalysts.

Herein, to address these issues, we report the synthesis and performance of a Fe–N–C catalyst featuring enriched FeN₄ sites and abundant micro/mesopores pores obtained through a feasible edge engineering strategy. This is achieved by the assistance of ammonium chloride (NH₄Cl) salt, which not only enables the preferential formation of FeN₄ sites and suppresses

Dr. X. Fu, Prof. L. Yang, Prof. Z. Bai
School of Chemistry and Chemical Engineering
Key Laboratory of Green Chemical Media and Reaction
Ministry of Education
Collaborative Innovation Center of Henan Province for
Fine Chemicals Green Manufacturing
Henan Normal University
Xinxiang 453007, China
E-mail: baizhengyu2000@163.com

 The ORCID identification number(s) for the author(s) of this article can be found under <https://doi.org/10.1002/aenm.201803737>.

DOI: 10.1002/aenm.201803737

Dr. X. Fu, B. Ren, Dr. G. Jiang, Dr. Y. Liu, Dr. F. M. Hassan,
Dr. J. Zhu, Z. P. Cano, Prof. A. Yu, Prof. Z. Chen
Waterloo Institute for Nanotechnology
Department of Chemical Engineering
University of Waterloo
200 University Ave. W, Waterloo, Ontario N2L 3G1, Canada
E-mail: zhwen@uwaterloo.ca
N. Li, Prof. D. Su
Center for Functional Nanomaterials
Brookhaven National Laboratory
Upton, NY 11973, USA
E-mail: dsu@bnl.gov

aggregates of other iron phases, but also creates abundant pores and nitrogen-doped edges within the in situ formed graphene matrix. The resulting pores play a vital role in not only promoting the intrinsic activity of single FeN₄ site as pointed out by density functional theory (DFT) calculations, but also in enhancing reactant accessibility to the active sites. Therefore, the obtained catalyst containing enriched edge-hosted FeN₄ sites exhibits remarkable catalytic activity for ORR in acid media and demonstrates superior performance in a practical H₂-air fuel cell.

A schematic diagram illustrating the catalyst synthesis is shown in **Figure 1**, with the full details of the experiments provided in the Supporting Information. In this approach, NH₄Cl was deliberately incorporated to modify the polymerization of the precursor mixture (Figure 1a). Next, the freeze-dried composite was subjected to an NH₄Cl salt-induced solid phase high temperature reaction (SPHTR) (Figure 1b), where the quantity and type of iron–nitrogen species as well as the morphology and structures of the carbon matrix are tailored. Then, the pyrolyzed materials were purified to obtain the final catalyst, which has a porous graphene-like mesh structure and is denoted as FeN_x/GM (Figure 1c). FeN_x-doped nonporous graphene-like nanoplatelet (FeN_x/GP) was also prepared as a reference, by omitting the use of NH₄Cl salt under otherwise identical conditions.

Here, NH₄Cl salt plays a crucial role in tailoring the surface chemistry and nanoarchitecture of the catalyst through its thermal decomposition reaction, in which a large amount of gases (NH₃ and HCl) are released. Specifically, NH₄Cl salt can be employed as a robust pore-forming agent for not only pore construction but also edge-site engineering, as further discussed below. Due to the lower thermal decomposition temperature compared to that of polyaniline (PANI) (Figure S1, Supporting Information), the abundant NH₄Cl salt within the catalyst precursors first starts to decompose and tends to release a significant amount of gases during pyrolysis activation. The trapped gases produce substantial internal stress and then expand the PANI phase which likely contributes to the formation of a pores architecture through graphenization during SPHTR.^[9] Thermogravimetric analysis (TGA) was performed to verify this interpretation. As depicted in Figure S1 in the Supporting Information, the NH₄Cl/PANI/FeCl₃/ammonium peroxodisulfate (APS) precursors exhibit a dramatic weight loss (≈55%) between 200 and 350 °C, showing very similar to that of pure NH₄Cl salt. By contrast, the PANI/FeCl₃/APS precursors show a more gradual weight loss, with only ≈25% below 350 °C and ≈72% until 900 °C, respectively. In addition, the released NH₃

could possibly etch the carbon matrix, increasing the porosity of the catalyst.^[10] On the other hand, NH₄Cl salt likely serves as an efficient nitrogen-doping agent as well, which is capable of tuning and enhancing the fraction of FeN₄ species in FeN_x/GM. This is exhibited by the increase of the overall nitrogen level in FeN_x/GM (5.36 at%) compared to FeN_x/GP (4.20 at%, Table S1, Supporting Information). The enhanced nitrogen content is likely to raise the tendency to anchor more iron atoms to generate active FeN_x sites (Table S2, Supporting Information).

The morphology of the Fe–N–C catalysts was first analyzed by transmission electron microscopy (TEM). The catalyst obtained without NH₄Cl salt displays an agglomerated bulk graphene-sheet-like structure consisting of ≈3 μm size platelets (**Figure 2a** and **Figure S2a–c**, Supporting Information). High-resolution transmission electron microscopy (HRTEM) images of the selected edge- and bulk-region in **Figure 2a** further indicate that the FeN_x/GP possesses an almost completely intact and nonporous carbon matrix (**Figure 2b,c** and **Figure S3a**, Supporting Information). In contrast, the combined FeN_x/GM shows a loose and more porous framework (**Figure 2d** and **Figure S2d–f**, Supporting Information). Moreover, the obtained graphene-like flakes are defective with nanosized holes across the plane (**Figure 2e,f** and **Figure S3b**, Supporting Information). The porosity of the obtained catalysts was further evaluated by the nitrogen adsorption–desorption technique. FeN_x/GM exhibits a relatively larger adsorption hysteresis loop (type-IV) at high pressure than that of FeN_x/GP, confirming that more abundant mesopores are formed in FeN_x/GM compared to FeN_x/GP (**Figure 2g**). Compared with FeN_x/GP, the specific surface area of FeN_x/GM is significantly enhanced (771 vs 1070 m² g⁻¹), indicating the pore-construction function of NH₄Cl during SPHTR. Further pore size distribution (**Figure 2g** (insert) and **Table S3**, Supporting Information) confirms the existence of hierarchical micro/mesopores in FeN_x/GM. Such large number of generated holes implies a relatively high structural disorder within the FeN_x/GM catalyst, which was further confirmed by a slightly higher I_D/I_G ratio of FeN_x/GM with respect to FeN_x/GP (1.12 vs 0.99) in the Raman spectra (**Figure 2h**). Moreover, a sharp and narrow (002) peak in the X-ray diffraction (XRD) pattern indicates a large number of graphitic domains in FeN_x/GM, whereas FeN_x/GP shows a much broader peak at ≈26° (**Figure 2i**). A high degree of graphitization is known to enhance the corrosion resistance of the carbon matrix and preserve the active sites.^[11]

This strategy also demonstrates a simple way to preferentially generate FeN₄ sites in Fe–N–C electrocatalysts, which is

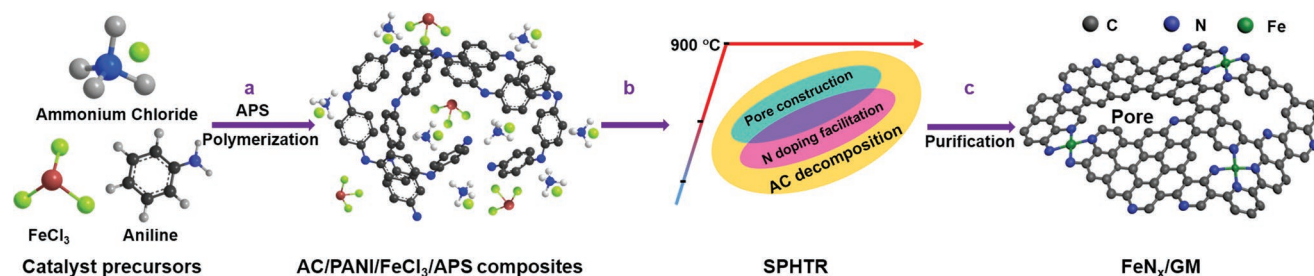


Figure 1. Synthetic scheme for the preparation of FeN_x/GM catalysts. a) Modification of the polymerization by the incorporation of NH₄Cl. b) NH₄Cl-induced SPHTR. c) Subsequent heat treatments and acid leaching processes.

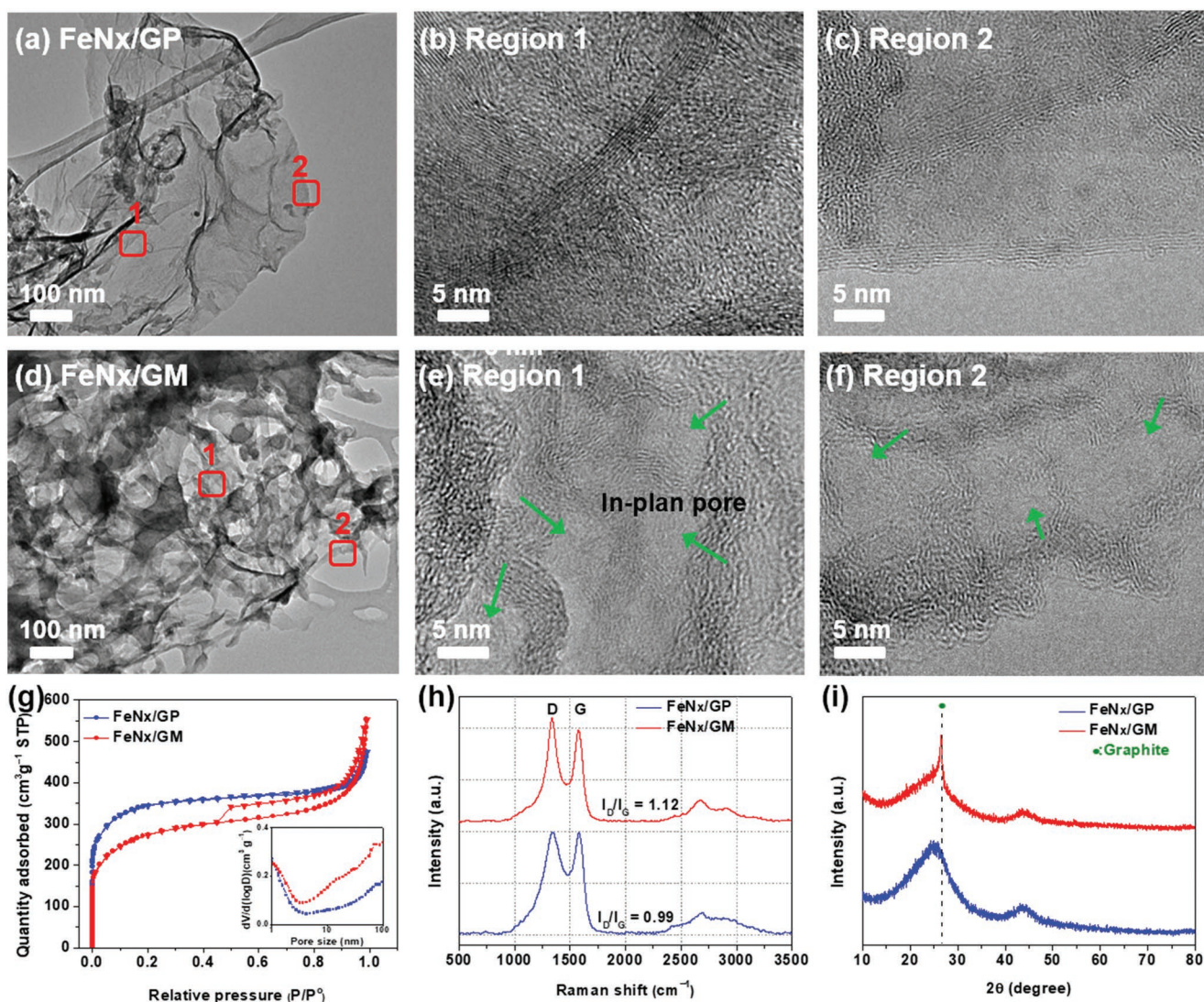


Figure 2. a) TEM and b,c) HRTEM of FeN_x/GP. d) TEM and e,f) HRTEM of FeN_x/GM. g) N₂ sorption isotherms of FeN_x/GP and FeN_x/GM; inset figure illustrates the pore size distribution. e) Raman spectra and i) XRD pattern of the prepared catalysts.

evident from several atomic-detection technologies. First, using the high-angle annular dark field scanning transmission electron microscopy (HAADF-STEM) (Figure 3a, Figure S4, and Figure S5a, Supporting Information) and corresponding electron energy loss spectroscopy (EELS) (Figure 3b and Figure S5b, Supporting Information), it is suggested that Fe atoms should be bonded with N atoms in the surroundings to form FeN_x moieties.^[12] It should be noted that a few scattered inorganic metallic particles were also detected and distributed randomly within the carbon support (Figure S6, Supporting Information). However, the TEM results only provide the general structure and composition of iron species in the two catalysts but cannot distinguish the overall proportion of FeN_x species.

X-ray absorption spectroscopy (XAS) was performed to investigate the local iron structure in both catalysts. The Fe K-edge X-ray absorption near edge structure (XANES) reveals that the two catalysts have a similar chemical state to FePC (Figure S7, Supporting Information), which is further confirmed from the

Fe K-edge extended X-ray absorption fine structure (EXAFS) in Figure 3c. From the shape and amplitude of the first strong peak at ≈ 1.5 Å, it is clear that the bonding environment in the first shell of these Fe–N–C samples is notably similar to that of FePC, suggesting that they more likely to contain FeN₄ complex structures.^[13] Besides, the peaks at ≈ 2.1 Å (assigned to Fe–Fe interactions) reveal the presence of iron-based crystalline structures in the two catalysts.^[14] Noticeably, the EXAFS spectrum of FeN_x/GM shows a higher peak intensity for Fe–N bonding and a lower intensity for Fe–Fe bonding compared to that of FeN_x/GP. Thus, the XAS results indicate that the introduced NH₄Cl salt promotes the enrichment of FeN₄ fraction in FeN_x/GM.

To gain deeper insight into the structure of Fe-related species in the FeN_x/GP and FeN_x/GM catalysts, ⁵⁷Fe Mössbauer spectroscopy was carried out (Figure 3d,e). The Mössbauer spectrum is fitted with two doublets, three sextets, and a singlet assigned to γ -Fe.^[4a,5a] The two doublets are assigned to FeN₄ moieties with Fe(II) in low- (D1) and medium-spin (D2) sites,

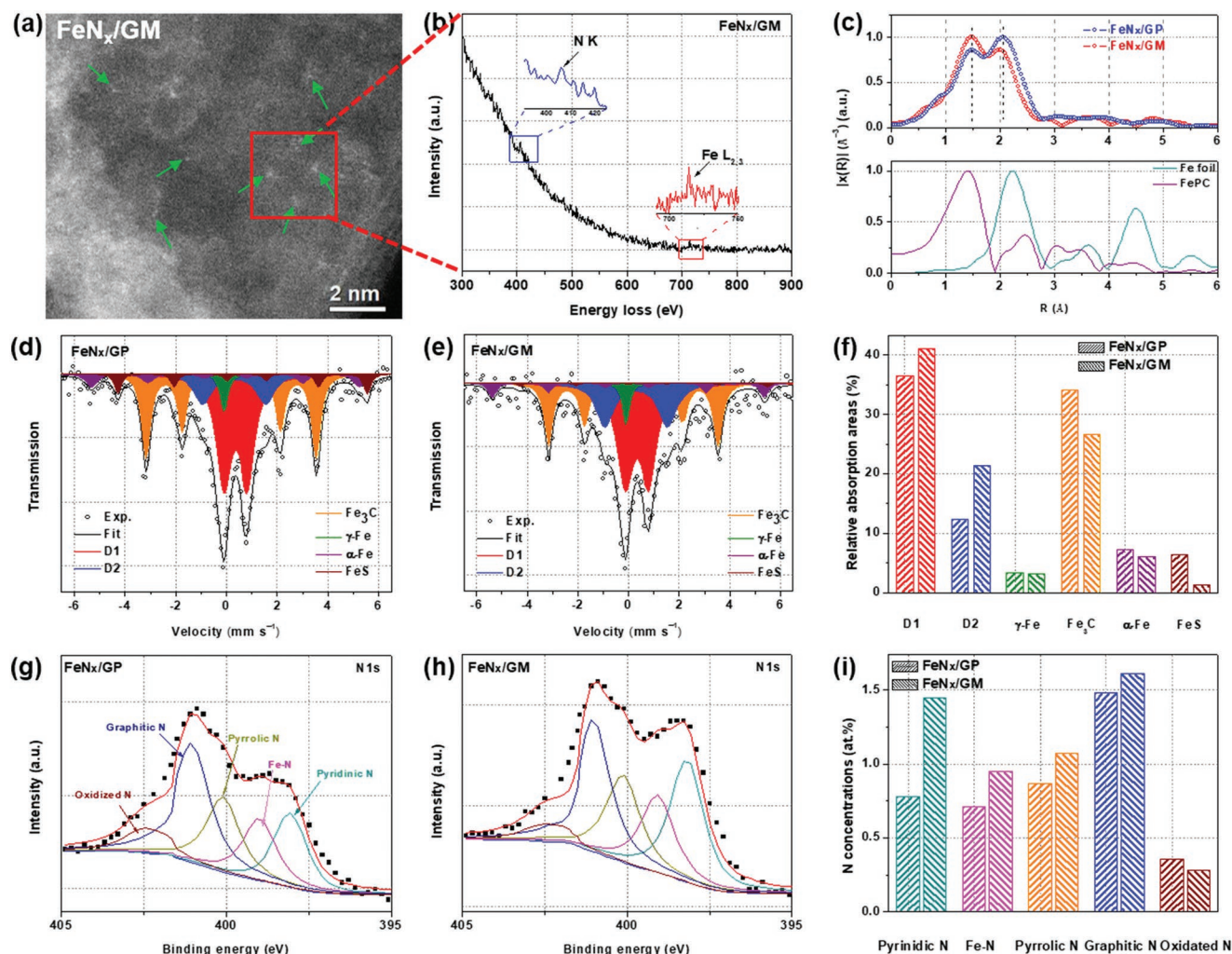


Figure 3. a) HAADF-STEM image of FeN_x/GM and b) EELS spectrum taken at the red rectangle selected area. c) Fe K-edge EXAFS spectra of prepared catalysts and references. d, e) ^{57}Fe Mössbauer spectra of prepared catalysts and f) category plots of the sum of relative absorption areas. g, h) XPS N1s spectra of prepared catalysts and i) change in the relative content of nitrogen species.

respectively, while the three sextets can be assigned to $\alpha\text{-Fe}$, FeS , and Fe_3C , respectively (Figure S4, Supporting Information). It is clear that the Mössbauer spectrum of FeN_x/GM exhibits a larger area for the doublet peaks than that of FeN_x/GP . In contrast, FeN_x/GP shows a higher proportion of the Fe_3C peak compared to FeN_x/GM . In Figure 2f, the relative absorption areas for all the assigned iron species were calculated. Specifically, the iron contents of the D1 and D2 species in FeN_x/GM are 41.13% and 21.43%, respectively, which are greater than the 36.53% and 12.28% contents in FeN_x/GP . The fraction of Fe_3C (26.65%) and FeS (1.27%) species are dramatically reduced in the FeN_x/GM catalyst compared to 34.15% and 6.43% in FeN_x/GP , respectively. In addition, the contents of $\gamma\text{-Fe}$ and $\alpha\text{-Fe}$ in the two catalysts are very similar (Table S4, Supporting Information). The large proportion of FeN_4 sites in FeN_x/GM could be ascribed to the enhanced nitrogen content that would anchor more iron atoms to generate FeN_x sites. Furthermore, the decline in the content of iron particles could also be linked to the function of NH_4Cl and was interpreted by a proposed mechanism in the Supporting Information

(Figure S8, Supporting Information). Mössbauer spectroscopy, which is performed on a large amount of the samples, provides a more comprehensive and accurate conclusion and thus proves that the two catalysts contain FeN_4 moieties, but with greater enrichment in FeN_x/GM .

X-ray photoelectron spectroscopy (XPS) was further performed to analyze the bonding information of nitrogen and iron (Figure S9 and Table S1, Supporting Information). The N 1s curves of the two catalysts can be deconvoluted into pyridinic-N, Fe-N, pyrrolic-N, graphitic-N, and oxalate-N bonded species (Figure 3g, h).^[15] The most notable difference between XPS analyses of the two catalysts is that the Fe-N content within FeN_x/GM is higher than that within FeN_x/GP (0.95 vs 0.69 at%), in line with the XAS and Mössbauer spectroscopy. Another notable point from the XPS spectra is that pyridinic-N accounts for 1.45 at% in FeN_x/GM , which is approximately two times higher than that in FeN_x/GP (0.78 at%) (Figure 3i and Table S2, Supporting Information). The dramatic enhancement of pyridinic-N suggests FeN_x/GM has highly exposed edge structures, which could provide more edge sites for nitrogen

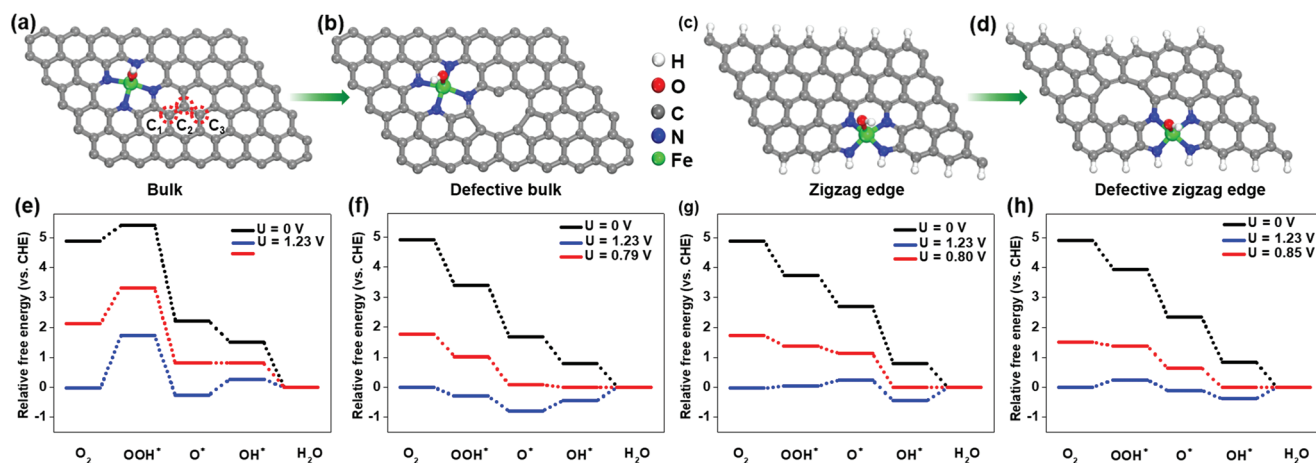


Figure 4. Model structures used in theoretical studies: a) bulk-, b) defective bulk-, c) zigzag edge-, and d) defective zigzag edge-hosted FeN_4 structures with OH ligands. e–h) Free energy diagram of the reduction of O_2 to H_2O on the above models. The endothermic adsorption reaction suggests this OH-modified bulk- FeN_4 configuration may not act as an active site on an associative ORR pathway.

incorporation, and therefore generates abundant edge-nitrogen (e.g., pyridinic-N) related FeN_x sites.

To gain further insight into the in-plane pore edge effect on the intrinsic activity of FeN_4 sites, we employed quantum chemical modeling to study the relevant ORR pathways on these sites with or without neighboring pore defects. Two types of representative FeN_4 models, including defective bulk- and defective zigzag-edge-hosted FeN_4 structures, and nondefective bulk- and nondefective zigzag-edge-hosted FeN_4 structures are illustrated in Figure 4a–d. Detailed descriptions are presented in the Supporting Information. We calculated the free energy change of each ORR step for the four models respectively at zero electrode potential ($U = 0$ V vs reversible hydrogen electrode (RHE)), the equilibrium potential ($U = 1.23$ V) and the potential for which all steps become energetically negative (thermodynamic limiting potential). It can be observed that the binding of intermediates O_2^* (0.44 eV) and OOH^* (0.43 eV) are endothermic on the bulk-hosted FeN_4 model (Figure 4e), which implies that this configuration may not act as a single reaction site on an associative ORR pathway and is in line with a previous report (Table S5, Supporting Information).^[16] On the other hand, the additional adjacent pore defect makes the FeN_4 structure exothermally bind O_2^* (−0.85 eV) and OOH^* (−1.75 eV), resulting in a thermodynamic limiting potential of 0.79 V (Figure 4f and Table S5, Supporting Information). Also, the introduced in-plane holes are more likely to further reduce the absorption energy of O_2^* and OOH^* from the nondefective edge (−0.27 and −0.35 eV) to the defective edge model (−0.16 and −1.20 eV), leading to an enhanced thermodynamic limiting potential (0.80 vs 0.85 V) (Figure 4g,h and Table S5, Supporting Information). These quantum chemistry calculations show that the proposed FeN_4 active sites when accompanied with adjacent pore defects lead to highly ORR-active structures. Thus, the FeN_x/GM catalyst featuring high porosity is more favorable for the ORR process and is therefore predicted to exhibit higher catalytic activity.

To investigate the edge-tailoring effects on the electrocatalytic performance, rotating ring-disk electrode (RRDE) tests of the prepared catalysts were conducted in 0.5 M H_2SO_4 . Both of

the two catalysts exhibit well-defined mass transport-limited current density; however, FeN_x/GM shows a more positive half-wave potential ($E_{1/2}$) than that of FeN_x/GP (0.80 vs 0.78 V) (Figure 5a), which is close to the state-of-the-art Pt/C catalyst (TKK, 28.2 wt%) as can be seen in Figure S10 in the Supporting Information. Additionally, ring-current values from RRDE measurements also verify that FeN_x/GM generates a slightly lower average H_2O_2 yield over the potential ranges from 0.80 to 0.20 V when compared to FeN_x/GP , corresponding to an average electron transfer number per O_2 molecule greater than 3.95 (Figure 5b). Further, to quantitatively compare their intrinsic activity, Tafel slopes and kinetic current density at 0.8 V are calculated through the Koutecky–Levich equation (Figure 5c).^[2e] It is clear that the Tafel slopes of the two catalysts show only marginal and nonsystematic differences (65 vs 72 mV dec^{-1}), whereas the addition of NH_4Cl salt leads to a significant enhancement of the kinetic current density by a factor of 2 (3.82 vs 1.97 mA cm^{-2} , Figure 5c (insert)). The values of the Tafel slopes reveal that the ORR mechanism of the two catalysts is almost similar. However, the larger proportion of FeN_4 sites coupled with the abundant pore structure in FeN_x/GM provide more active and accessible catalytic sites to participate in ORR (Figure S11, Supporting Information), leading to the improved kinetic current density. These electrochemical results clearly show that edge engineering in this work confers boosted ORR activity on the Fe–N–C catalyst.

Evaluation of M–N–C catalysts under realistic fuel cell operation, particularly in H_2 –air conditions, is more meaningful for their validation yet is challenging.^[17] The main problem is that the oxygen transfer resistance, a key factor that dictates the PEMFC performance, is more severe in a complete cell than in an oxygen-saturated solution due to the low oxygen percentage in air. Porosity construction by the assistance of NH_4Cl salt can be a feasible way to address this issue. As expected, the addition of higher amounts of NH_4Cl salt (from 10 to 60 wt%) clearly improves the ORR performance, but these NH_4Cl derived catalysts show similar ORR activity in RDE measurements (half-wave potential differences <10 mV, Figure S12a, Supporting Information). Compared with FeN_x/GP , the improved

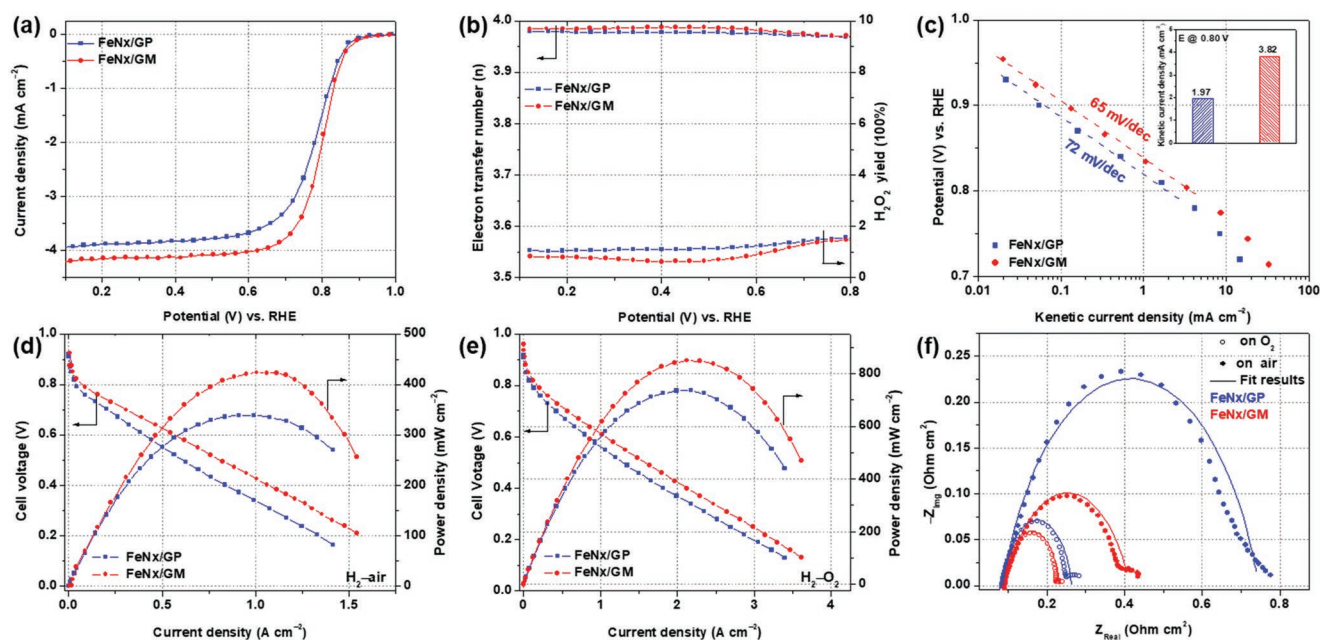


Figure 5. a) Steady-state ORR polarization plots and b) electron transfer number and H_2O_2 yield of prepared catalysts. c) Tafel plots and the comparison of kinetic current at 0.80 V (insert). All the RDE/RRDE test conditions: 0.5 M H_2SO_4 saturated with O_2 , 900 rpm, catalyst loading of 0.6 mg cm^{-2} . Polarization and power density as the functions of the current density plots for d) H_2 -air and e) H_2 - O_2 PEMFC with the prepared materials as the cathode catalysts. Membrane: Nafion 211, cathode catalyst loading: 4 mg cm^{-2} , anode: $0.2 \text{ mg}_{\text{Pt}} \text{ cm}^{-2}$ Pt, O_2/air and H_2 : 300 sccm, backpressure: 20 psig, cell and fuel gas temperatures: 80°C ; ionomer to catalyst weight ratio = 1/5; electrode area 5 cm^2 . f) Nyquist plots for PEMFCs at 0.60 V.

ORR activity of NH_4Cl salt-assisted catalysts could be mainly attributed to the boost in overall nitrogen content, which would generate more FeN_4 active sites (Table S6, Supporting Information). However, it is important to note that the conventional RDE measurements do not capture the variation of oxygen transfer resistance through the electrode, which is crucial for fuel cell operation. By contrast, H_2 -air fuel cell polarization curves of AC derived catalysts are distinct in the high current density region, where higher AC content leads to less voltage loss by increasing the current density (Figure S12 b, Supporting Information), indicating improved fuel cell performance. This enhancement could be ascribed to the increased specific surface area and pore structure (Table S6, Supporting Information) which tend to facilitate active sites accessibility and promote their utilization, resulting in improved transport properties and superior fuel cell performance. However, too much NH_4Cl salt (60 wt%) does not impart much improved fuel cell performance, probably due to the fact that the active sites utilization has already reached the maximum state and additional surface area may not be accessed by the reactants. Thus, we suggest that the catalyst prepared with 50 wt% NH_4Cl (namely, FeN_x/GM) exhibits the highest fuel cell performance, and all the physical characterization and electrochemical measurements presented above were obtained on this catalyst. Owing to the synergic effects of enriched FeN_4 moieties and abundant porosity, the FeN_x/GM catalyst demonstrates excellent fuel cell performance in air. At a working voltage of 0.6 V, the cathode made with FeN_x/GM exhibits a power density of 0.35 W cm^{-2} , 150% higher than that of the cathode fabricated with FeN_x/GP (0.23 W cm^{-2}) (Figure 5d). Moreover, the maximum power density (P_{max}) of the cell with FeN_x/GM reaches a remarkable value

of 0.43 W cm^{-2} , significantly superior to that of 0.34 W cm^{-2} for FeN_x/GP . Such a high output power density is able to reach approximately 58% of the P_{max} (0.6 W cm^{-2}) of Pt cathode ($0.2 \text{ mg}_{\text{Pt}} \text{ cm}^{-2}$) operated under the same conditions (Figure S13, Supporting Information), which is among the best reported in the literature for the M-N-C catalysts measured under practical H_2 -air conditions (Table S7, Supporting Information).^[3b,16,18] In addition, experiments under H_2 - O_2 conditions were also conducted for contrast to highlight the importance of pore-engineering for boosting fuel cell performance. As expected, FeN_x/GM again presents superior performance to FeN_x/GP , with increased power density at 0.6 V (0.64 vs 0.51 W cm^{-2}) as well as P_{max} (0.86 vs 0.74 W cm^{-2}) (Figure 5e). Electrochemical impedance spectroscopy (EIS) was carried out to further display the advantage of edge engineering (Figure 5f and Figure S14, Supporting Information). It is noticeable that FeN_x/GM cathodes exhibit much smaller charge transfer resistance in both air ($0.32 \Omega \text{ cm}^{-2}$) and neat oxygen ($0.14 \Omega \text{ cm}^{-2}$) vs those of FeN_x/GP (0.68 and $0.18 \Omega \text{ cm}^{-2}$, respectively, Table S8, Supporting Information). We speculate that the large number of active sites coupled with abundant mesopores promote charge transfer and diffusion of O_2 to the active sites, contributing to the efficient electrochemical active cathode and excellent fuel cell performances. In addition, the durability of the electrodes made with FeN_x/GP and FeN_x/GM catalysts were investigated and shown in Figure S15 in the Supporting Information.

In summary, edge engineering is demonstrated and explored for multituning of a Fe-N-C catalyst by an NH_4Cl assisted approach. This feasible strategy realizes simultaneous generation of a high proportion of FeN_4 species and an abundant and favorable pore structure in the catalyst. Furthermore,

DFT calculations suggest that the pore-edge-effect promotes the intrinsic activity of the FeN₄ configuration. Moreover, the PEMFC using this catalyst at the cathode exhibits smooth charge/mass transfer properties and delivers impressive P_{\max} values of 0.43 W cm⁻² under air conditions. This work, therefore, provides a new avenue for obtaining highly active ORR electrocatalysts and boosting PEMFC performance through edge tailoring the FeN₄ site.

Supporting Information

Supporting Information is available from the Wiley Online Library or from the author.

Acknowledgements

This research was supported by the University of Waterloo. The Catalysis Research for Polymer Electrolyte Fuel Cells (CaRPE FC) Network administered from Simon Fraser University and supported by Automotive Partnership Canada (APC) Grant no. APCPJ 417858-11 through the Natural Sciences and Engineering Research Council of Canada (NSERC) are greatly acknowledged. Electron Microscopy (EM) work used resources of the Center for Functional Nanomaterials, which is a US DOE Office of Science Facility, at Brookhaven National Laboratory under Contract No. DE-SC0012704. This work was also financially supported by the National Natural Science Foundation of China (Grant No. 51872075), the 111 Project (Grant No. D17007), and Henan Center for Outstanding Overseas Scientists (Grant No. GZS2018003).

Conflict of Interest

The authors declare no conflict of interest.

Keywords

edge engineering, FeN₄ sites, fuel cells, M–N–C catalysts, oxygen reduction reaction

Received: December 3, 2018
Revised: January 12, 2019
Published online:

- [1] a) M. Winter, R. J. Brodd, *Chem. Rev.* **2004**, *104*, 4245; b) M. K. Debe, *Nature* **2012**, *486*, 43.
- [2] a) S. Chen, Z. Wei, X. Qi, L. Dong, Y.-G. Guo, L. Wan, Z. Shao, L. Li, *J. Am. Chem. Soc.* **2012**, *134*, 13252; b) B. Y. Xia, H. B. Wu, N. Li, Y. Yan, X. W. Lou, X. Wang, *Angew. Chem., Int. Ed.* **2015**, *54*, 3797; c) N. Cheng, M. N. Banis, J. Liu, A. Riese, X. Li, R. Li, S. Ye, S. Knights, X. Sun, *Adv. Mater.* **2015**, *27*, 277; d) M. A. Hoque, F. M. Hassan, D. Higgins, J.-Y. Choi, M. Pritzker, S. Knights, S. Ye, Z. Chen, *Adv. Mater.* **2015**, *27*, 1229; e) H. A. Gasteiger, S. S. Kocha, B. Sompalli, F. T. Wagner, *Appl. Catal., B* **2005**, *56*, 9.
- [3] a) Q. Wang, Z.-Y. Zhou, Y.-J. Lai, Y. You, J.-G. Liu, X.-L. Wu, E. Terefe, C. Chen, L. Song, M. Rauf, N. Tian, S.-G. Sun, *J. Am. Chem. Soc.* **2014**, *136*, 10882; b) X. Fu, P. Zamani, J.-Y. Choi, F. M. Hassan, G. Jiang, D. C. Higgins, Y. Zhang, M. A. Hoque, Z. Chen, *Adv. Mater.* **2017**, *29*, 1604456; c) A. Serov, K. Artyushkova, P. Atanassov, *Adv. Energy Mater.* **2014**, *4*, 1301735; d) M. Lefèvre, E. Proietti, F. Jaouen, J.-P. Dodelet, *Science* **2009**, *324*, 71; e) G. Wu, K. L. More, C. M. Johnston, P. Zelenay, *Science* **2011**, *332*, 443.
- [4] a) U. I. Kramm, M. Lefèvre, N. Larouche, D. Schmeisser, J.-P. Dodelet, *J. Am. Chem. Soc.* **2014**, *136*, 978; b) A. Zitolo, V. Goellner, V. Armel, M.-T. Sougrati, T. Mineva, L. Stievano, E. Fonda, F. Jaouen, *Nat. Mater.* **2015**, *14*, 937; c) C. Zhu, Q. Shi, B. Z. Xu, S. Fu, G. Wan, C. Yang, S. Yao, J. Song, H. Zhou, D. Du, S. P. Beckman, D. Su, Y. Lin, *Adv. Energy Mater.* **2018**, *8*, 1801956; d) X. X. Wang, D. A. Cullen, Y.-T. Pan, S. Hwang, M. Wang, Z. Feng, J. Wang, M. H. Engelhard, H. Zhang, Y. He, Y. Shao, D. Su, K. L. More, J. S. Spendelow, G. Wu, *Adv. Mater.* **2018**, *30*, 1706758; e) Q. Jia, N. Ramaswamy, U. Tylus, K. Strickland, J. Li, A. Serov, K. Artyushkova, P. Atanassov, J. Anibal, C. Gumecci, S. C. Barton, M.-T. Sougrati, F. Jaouen, B. Halevi, S. Mukerjee, *Nano Energy* **2016**, *29*, 65.
- [5] a) M. Ferrandon, A. J. Kropf, D. J. Myers, K. Artyushkova, U. Kramm, P. Bogdanoff, G. Wu, C. M. Johnston, P. Zelenay, *J. Phys. Chem. C* **2012**, *116*, 16001; b) Y. J. Sa, D.-J. Seo, J. Woo, J. T. Lim, J. Y. Cheon, S. Y. Yang, J. M. Lee, D. Kang, T. J. Shin, H. S. Shin, H. Y. Jeong, C. S. Kim, M. G. Kim, T.-Y. Kim, S. H. Joo, *J. Am. Chem. Soc.* **2016**, *138*, 15046.
- [6] Z. W. Chen, D. Higgins, A. P. Yu, L. Zhang, J. J. Zhang, *Energy Environ. Sci.* **2011**, *4*, 3167.
- [7] E. F. Holby, G. Wu, P. Zelenay, C. D. Taylor, *J. Phys. Chem. C* **2014**, *118*, 14388.
- [8] a) E. Antolini, *Appl. Catal., B* **2009**, *88*, 1; b) E. Proietti, F. Jaouen, M. Lefèvre, N. Larouche, J. Tian, J. Herranz, J.-P. Dodelet, *Nat. Commun.* **2011**, *2*, 416; c) X. Fu, F. M. Hassan, P. Zamani, G. Jiang, D. C. Higgins, J.-Y. Choi, X. Wang, P. Xu, Y. Liu, Z. Chen, *Nano Energy* **2017**, *42*, 249; d) J. Shui, C. Chen, L. Grabstanowicz, D. Zhao, D.-J. Liu, *Proc. Natl. Acad. Sci. USA* **2015**, *112*, 10629.
- [9] G. Wu, N. H. Mack, W. Gao, S. Ma, R. Zhong, J. Han, J. K. Baldwin, P. Zelenay, *ACS Nano* **2012**, *6*, 9764.
- [10] a) F. Jaouen, M. Lefèvre, J.-P. Dodelet, M. Cai, *J. Phys. Chem. B* **2006**, *110*, 5553; b) F. Jaouen, J.-P. Dodelet, *J. Phys. Chem. C* **2007**, *111*, 5963.
- [11] W. Zhang, P. Sherrell, A. I. Minett, J. M. Razal, J. Chen, *Energy Environ. Sci.* **2010**, *3*, 1286.
- [12] H. Zhang, S. Hwang, M. Wang, Z. Feng, S. Karakalos, L. Luo, Z. Qiao, X. Xie, C. Wang, D. Su, Y. Shao, G. Wu, *J. Am. Chem. Soc.* **2017**, *139*, 14143.
- [13] H. J. Choi, G. Kwag, S. Kim, *J. Electroanal. Chem.* **2001**, *508*, 105.
- [14] U. I. Kramm, J. Herranz, N. Larouche, T. M. Arruda, M. Lefèvre, F. Jaouen, P. Bogdanoff, S. Fiechter, I. Abs-Wurmbach, S. Mukerjee, J.-P. Dodelet, *Phys. Chem. Chem. Phys.* **2012**, *14*, 11673.
- [15] F. Jaouen, J. Herranz, M. Lefèvre, J.-P. Dodelet, U. I. Kramm, I. Herrmann, P. Bogdanoff, J. Maruyama, T. Nagaoka, A. Garsuch, J. R. Dahn, T. Olson, S. Pylypenko, P. Atanassov, E. A. Ustinov, *ACS Appl. Mater. Interfaces* **2009**, *1*, 1623.
- [16] H. T. Chung, D. A. Cullen, D. Higgins, B. T. Sneed, E. F. Holby, K. L. More, P. Zelenay, *Science* **2017**, *357*, 479.
- [17] United States Department of Energy, **2017** Annual Progress Report—Catalysts and Electrodes, https://www.hydrogen.energy.gov/pdfs/review17/fc160_zelenay_2017_o.pdf (accessed: November 2018).
- [18] a) N. Larouche, R. Chenitz, M. Lefèvre, E. Proietti, J.-P. Dodelet, *Electrochim. Acta* **2014**, *115*, 170; b) A. Serov, M. J. Workman, K. Artyushkova, P. Atanassov, G. McCool, S. McKinney, H. Romero, B. Halevi, T. Stephenson, *J. Power Sources* **2016**, *327*, 557; c) J. Tian, A. Morozan, M. T. Sougrati, M. Lefèvre, R. Chenitz, J.-P. Dodelet, D. Jones, F. Jaouen, *Angew. Chem., Int. Ed.* **2013**, *52*, 6867; d) P. Zamani, D. C. Higgins, F. M. Hassan, X. Fu, J.-Y. Choi, M. A. Hoque, G. Jiang, Z. Chen, *Nano Energy* **2016**, *26*, 267; e) J. Wang, Z. Huang, W. Liu, C. Chang, H. Tang, Z. Li, W. Chen, C. Jia, T. Yao, S. Wei, Y. Wu, Y. Li, *J. Am. Chem. Soc.* **2017**, *139*, 17281.